# Influence on microstructure, strength and ductility of build platform temperature during laser powder bed fusion of AlSi10Mg

Juan Guillermo Santos Macías, Thierry Douillard, Lv Zhao, Éric Maire, Grzegorz Pyka, Aude Simar

**To cite this version:**

Juan Guillermo Santos Macías, Thierry Douillard, Lv Zhao, Éric Maire, Grzegorz Pyka, et al.. Influence on microstructure, strength and ductility of build platform temperature during laser powder bed fusion of AlSi10Mg. Acta Materialia, 2020, 201, pp.231-243. 10.1016/j.actamat.2020.10.001 . hal-03154980

**HAL Id: hal-03154980**

**https://hal.science/hal-03154980v1**

Submitted on 2 Jun 2022

# Influence on microstructure, strength and ductility of build platform temperature during laser powder bed fusion of AlSi10Mg

Juan Guillermo Santos Macías[a,*], Thierry Douillard[b], Lv Zhao[a,c,d], Eric Maire[b], Grzegorz Pyka[a], Aude Simar[a]

[a]*Université catholique de Louvain, Institute of Mechanics, Materials and Civil Engineering, IMAP, B-1348 Louvain-la-Neuve, Belgium*
[b]*Université de Lyon, Mateis, INSA Lyon, UMR5510 CNRS, F-69621 Villeurbanne, France*
[c]*Department of Mechanics, Huazhong University of Science and Technology, Wuhan, China*
[d]*Hubei Key Laboratory of Engineering Structural Analysis and Safety Assessment, Wuhan, China*
*Corresponding author. *E-mail address:* juan.santos@uclouvain.be. Postal address: Place Ste Barbe 2 L5.02.02 Louvain-la-Neuve, Belgium 1348. Phone number: +3210472490

## Abstract

AlSi10Mg manufactured by laser powder bed fusion (or selective laser melting) benefits from a very fine microstructure that imparts significant mechanical strength to the material compared to the cast alloy. The build platform temperature stands out as a significant processing parameter influencing the microstructure as it affects the cooling rate and thermal gradient during manufacturing. Setting the build platform temperature to 200°C yields a negligible residual stress level. However, the strength is lower compared to that obtained using a build platform temperature of 35°C, with a similar fracture strain. A detailed 3D microstructural analysis involving focused ion beam/scanning electron microscopy tomography was performed to describe the connectivity and size of the Si-rich eutectic network and link it to the strength and fracture strain. The coarser microstructure of the 200°C build platform material is more prone to damage. The α-Al cells as well as the Si-rich precipitates present a larger size in the 200°C material, the latter thus having a lower strengthening effect. The Si-rich eutectic network is also less interconnected and has a larger thickness in the 200°C material. An analytical model is developed to exploit these microstructural features and predict the strength of the two materials.

## *Keywords*

Laser powder bed fusion, aluminium alloy, microstructure, strengthening mechanism, damage initiation

## 1. Introduction

The relatively novel additive manufacturing (AM) area represents a great potential for various applications and industries, but it also involves important scientific challenges. In the case of metal AM, its attractiveness is important in structural applications for the aeronautic and aerospace industries. AM aluminium alloys are specially interesting in these lightweight applications, laser powder bed fusion (LPBF) AlSi10Mg being a common material and process combination [1-3]. Note that selective laser melting remains a rather common trade name for the LPBF technology.

There is a strong demand for high performing structural parts that can allow for further improvements, leading to decrease in weight and fuel consumption. AM can be a powerful tool in this endeavour, but, in order to represent a significant and highly attractive leap forward, its design flexibility has to be accompanied by an enhancement in mechanical performance. To achieve this, a thorough understanding from the materials science point of view of the AM parts has to be acquired [4].

In fact, various research efforts have been devoted to lightweight metal AM, with a focus on Ti6Al4V and AlSi10Mg. The latter is a very good example of the AM potential which has already found its application in the aeronautic industry. The technology allows to produce unique complex lattice structures and the material exhibits very good static mechanical performance [5]. Compared to the same alloy produced by casting, the LPBF counterpart offers an improvement of 167% in mechanical strength and of 74% in ductility (for a build platform temperature of 35°C for the LPBF material); see Fig. 1, which reports the tensile stress - strain curves for as cast and as built LPBF AlSi10Mg. The high cooling rate of the LPBF process yields a totally different and much finer microstructure than casting [6].

The tensile properties are known to be affected by the LPBF processing parameters [7]. In particular, here it is found that with a build platform temperature of 200°C the fracture strain is not improved while the strength is significantly decreased; see Fig. 1. This difference deserves some in-depth analysis to relate it to the microstructural features and in particular to the strengthening Si-rich network, which has been found to be the main damage initiation site [8]. Considering practical applications, the use of a higher build platform temperature is still relevant, since the part presents almost no residual stresses, while they were found to reach 50 MPa in tension with a 35°C build platform temperature. These residual stress levels were measured in previous work [9] for identical samples as the ones for which the mechanical properties are provided in Fig. 1.

Previous studies have investigated the microstructure and the mechanical behaviour of LPBF AlSi10Mg manufactured with build platform temperature of 35°C or 200°C separately, but the comparative investigation of both materials to determine the differences between the microstructures and their origin and relation to the mechanical behaviour is very limited. Awd et al. [10] have studied the mechanical behaviour of LPBF AlSi10Mg fabricated with build platform temperatures of 35°C and 200°C. Their research nearly exclusively focused on the fatigue aspects and was thus mainly aimed at the influence of porosity. Indeed, the effect of porosity is more critical than that of the microstructure in cyclic loading regime. Buchbinder et al. [11] revealed degraded mechanical properties of LPBF AlSi10Mg with a build platform temperature of 220°C. However the microstructure was not thoroughly characterised. It is therefore pertinent to address the microstructural aspects and their variation with the build platform temperature, especially with the aim of unveiling the origin of the static mechanical behaviour observed in Fig. 1.

Regarding the microstructure of LPBF AlSi10Mg, it is now well established [12,13] that it is composed of an α-Al cellular phase and a Si-rich eutectic phase. This microstructure is sometimes called “pseudoeutectic” [13] due to its metastability and to the far from equilibrium conditions at which it is originated. Indeed, the LPBF process is characterised by very fast and local heating, which is followed by rapid cooling and solidification under high thermal gradient [14] leading to a very fine metastable microstructure. The build platform temperature can have an impact on the thermal gradient during the cooling down of the material, influencing the microstructure. Due to the layer by layer building strategy, the microstructure of LPBF AlSi10Mg presents three distinguishable zones, i.e., fine melt pool (FMP) zone, coarse melt pool (CMP) zone and heat affected zone (HAZ), according to the morphology and size of the Si-rich eutectic phase [14]. In the FMP and CMP the Si-rich eutectic phase exhibits a network feature with high interconnection, while in the HAZ this network is broken down [12,14]. Liu et al. [13] associated the formation of the CMP zone to the semisolid zone of the melt pool, i.e., corresponding to the partially remelted zone of the previous layer. Previous studies investigated the microstructure mostly with two-dimensional (2D) scanning electron microscopy (SEM) images, which present limitations on unveiling the full morphology of the Si-rich eutectic phase. The three-dimensional (3D) characterisation proposed in the present study is therefore desirable to capture the microstructural differences resulting from different build platform temperatures and, in particular, its connectivity level for various zones.

The significant strength of as built LPBF AlSi10Mg is owed to the very fine microstructure and its specific morphology. The interconnected Si-rich eutectic network can act as load carrier and as a barrier hindering dislocation motion, leading to a significant strengthening effect [15]. The alteration of this microstructure through thermal inputs can result in its coarsening and globularisation, accompanied by a consequent weakening of the material [8,16]. It is therefore expected that a change in build platform temperature will impact the microstructure-mechanical behaviour conjunction.

This study aims at establishing the correlation between microstructure and mechanical strength and ductility, with a special focus on the morphological and the damage mechanism aspects and their alteration occurring just with the modification of the build platform temperature. Both 2D and 3D microstructure characterisations were performed with SEM and focused ion beam (FIB)/SEM tomography, respectively. The damage mechanism and its relation to microstructure was revealed with SEM observation. Moreover, the mechanical strength was analysed with microstructure-fed strengthening models in the light of which damage behaviour and ductility were discussed.

## 2. Experimental methods

The LPBF material was manufactured with an EOS M290 metal AM system. Two different build platform temperatures were used, 35°C and 200°C, with very similar sets of optimised parameters suggested by the machine manufacturer; see [17,18] for more details. Parts were printed in the form of 5x35x150 mm plates on lattice supports. Microscopy analysis and horizontally oriented mechanical testing samples were extracted from these plates. The orientation of these mechanical testing samples in the LPBF plates is depicted in Fig. 2, and the x, y, z coordinate system will be reused in following figures for better readability of the sample orientation.

Table 1 provides the chemical composition of the LPBF built parts determined by inductively coupled plasma optical emission spectroscopy (ICP OES), as well as that of the cast material from which the samples were extracted for the cast tensile test results presented in Fig. 1. The chemical composition of the LPBF built parts is similar, indicating that the change in build platform temperature does not cause any loss of alloying elements.

Classical 2D mesostructural and microstructural analyses were performed using optical microscopy (OM) and scanning electron microscopy (SEM, Zeiss supra 55VP and Zeiss ultra 55), respectively. Electron backscatter diffraction (EBSD) characterisation was also performed (Zeiss supra 55VP). Prior to observation, samples were polished with a final step of active oxide polishing solution (OPS) and lightly etched with an 0.5 vol% HF solution. The accelerating voltage was set to 20 kV and the current to 7 nA. EBSD maps were acquired with a Symmetry detector and data were post-processed with HKL Channel5 software (Oxford Instruments, Abingdon, UK) to suppress the non-indexed points without affecting the orientation of their neighbours. EBSD mapping was performed at 200 Hz with a step of 500 nm, on 550x410 µm and 430x340 µm areas for the build platform temperatures of 35°C and 200°C, respectively.

To obtain 3D volumes of the studied materials, SEM was coupled with the focused ion beam (FIB) milling technique (Zeiss NVision 40 workstation combining a Seiko SIINT zeta FIB column with a Gemini I SEM column). The angle between the FIB and SEM columns was 54°. Before running the acquisition, a carbon layer (6x6x1 µm) was deposited on an area of interest by in situ ion beam induced deposition (IBID) to further smooth out the surface roughness during slicing in order to achieve sharp upper edges and minimise curtaining artefacts (i.e., vertical stripes on the cross section induced by ion milling and partly due to the sensitivity of the sputtering yield with respect to the angle of incidence and to the phases). Then, several reference lines were imprinted into the carbon layer and filled in situ with wolfram for reliable post-stack alignment purposes. A sample prepared for FIB/SEM tomography imaging is depicted in Fig. 3. After acquiring an SEM 2D image, a 5 nm layer of material was removed using FIB. Serial FIB sectioning was done with a current of 700 pA at 30 keV. The following SEM 2D image was acquired and this process was repeated several hundred times to obtain a SEM 3D volume with a resolution of 5 nm. This process was carried out using the FIBICS Atlas3D scan generator and image acquisition system.

Uniaxial tensile testing was performed following the ASTM E8/8M - 15a standard to characterise the static tensile behaviour of the materials. Round tensile specimens were machined from the bulk cast or LPBF materials (Fig. 2). Their orientation was parallel with regards to the LPBF building platform. A minimum of four samples were tested for each condition. For the LPBF materials, tensile specimens were extracted at three different heights in a plate and no influence of the height level was observed. The results were already provided in the introduction (Fig. 1) as motivation for this work. Fractography analysis of the fracture surface of the tensile specimens was conducted using SEM to achieve a more thorough understanding of the damage mechanisms. To further analyse damage the mid-section along the longitudinal plane of the tested tensile samples was observed after surface preparation. Damage characterisation was achieved using the ImageJ software on SEM micrographs.

## 3. Results

### 3.1. Melt pool and grain mesostructure

The mesostructure of the LPBF material can be characterised with OM. The melt pool structure that constitutes the alloy is provided in Fig. 4. These melt pools are left by the laser beam as it advances melting the freshly deposited metal powder layer and part of the previously solidified layers, also thermally affecting a small area around the melted material. As mentioned in the introduction, the melt pools contain two peripheral layers, the heat affected zone (HAZ) and the coarse melt pool (CMP) zone, forming the melt pool border that can be identified in Fig. 4b,d. The fine melt pool (FMP) zone constitutes the rest of the melt pool structure.

Table 2 presents a summary of the melt pool structure dimensions as defined in the schematic drawing of Fig. 4e. The melt pools have a similar mean size for both build platform temperatures, although slight differences were measured. The disparity can be linked to the fact that the HAZ and CMP are both twice as thick in the 200°C build platform temperature material compared to the 35°C one, resulting consequently in a melt pool border of double thickness.

The nature, shape and distribution of the grains are related to this melt pool mesostructure. The grain size and orientation can be seen in the EBSD colour maps depicted in Fig. 5a,b together with the grain size distribution (Fig. 5e). The associated pole figures are also provided in Fig. 5c,d. It is clear from Fig. 5a,b that there is a link between the melt pool mesostructure and grain shape, size, distribution and orientation. Indeed, two grain populations can be distinguished on the distribution of Fig. 5e. The first one consists of columnar grains that grow in a radial fashion from the melt pool border towards its centre following the thermal gradient, with a preferential growth in the building direction. These epitaxial grains can extend through several melt pools since they are already present just below when melting the subsequent layer and will act as nucleation sites. The second population is composed of very small equiaxial grains along melt pool borders akin to the ones found in the chill zone of a weld [19] or a cast part, indicative of heterogeneous nucleation [20]. In the 200°C build platform temperature material the second grain population is less abundant and of a larger size.

The pole figures of Fig. 5c,d show that a <100> fibre texture is clearly present in these materials as already evidenced by Thijs et al. [14] for the same alloy manufactured by LPBF. The pole figures of the 35°C and 200°C materials do not show any evidence of difference in texture between the two.

Therefore, the differences in grain size and texture are not very significant and cannot by themselves explain the difference in mechanical behaviour between the 35°C and 200°C materials that is found in Fig. 1. It is thus necessary to delve deeper into the microstructure to understand the origin of the differences.

### 3.2. Cellular structure characterisation

Fig. 6a,b presents the 2D SEM characterisation of the FMP zone microstructure composed of a Si-rich eutectic phase forming a network that surrounds the α-Al cells. The dark zones correspond to the α-Al cells, enveloped by the lighter features that constitute the Si-rich eutectic network. Fig. 6c,d shows that, inside these cells forming the matrix of the microstructure, Si-rich precipitates are present. This has already been shown in LPBF AlSi10Mg produced in similar conditions [8]. In the case of 200°C build platform temperature these precipitates present a larger size and some of them exhibit a needle shape.

The FMP zone occupies most of the volume of the material. Its microstructure can therefore be considered the most representative of the material. However, the CMP and HAZ present specific particularities, as will be described in the next paragraph. Fig. 7a,b shows the CMP zone, which is similar to the FMP, but with a larger cell size.

The HAZ, forming together with the CMP the melt pool border, can be observed in Fig. 7c,d. The HAZ has the lowest thickness of the three melt pool zones. The Si-rich eutectic phase appears more fragmented in the HAZ (this will be shown clearly later in Table 3), particularly for the 200°C build platform temperature material.

Although the 2D analysis provides abundant information on the microstructure of the materials, it is limited in some aspects, especially to evaluate the morphology. To reach a comprehensive characterisation a 3D rendering is necessary. Taking into consideration the limitations of the 2D microstructure analysis, SEM was coupled with FIB to perform 3D imaging of the material. The selected 5 nm resolution allows proper characterisation of the Si-rich eutectic. The geometry of this phase in the FMP zones of 35°C and 200°C build platform temperature samples can be observed in Fig. 8a,b, respectively (see Fig. 8c,d for more detail).

The FMP Si-rich eutectic phase forms a 3D network surrounding the α-Al matrix (Fig. 8; Si-rich eutectic network is visualised in red). The branches of the network are more plate than rod-shaped. The spaces inside the network filled by the α-Al cells can be described as elongated, tubular, but, due to the plate-like shape of the Si-rich eutectic, the perimeters of the cells are faceted instead of being perfectly round. The Si-rich precipitates inside the Al matrix are observable in the 200°C build platform material and highlighted in blue; see Fig. 8b,d. They are also present on the 35°C case (see Fig. 6c), but they are finer and cannot be properly detected with the FIB/SEM performed in this study. Fig. 8b,d confirms the presence of two populations of Si particles in the 200°C material, one being round and the other needle-shaped.

A comprehensive characterisation of LPBF AlSi10Mg logically has to take into consideration the three different melt pool zones. A volume at the melt pool border was scanned to obtain information on the CMP and HAZ. Fig. 9a,b,c presents smaller subvolumes of three 3D tomographies containing each the Si-rich eutectic phase of one of the 3 melt pool zones for the 35°C build platform temperature. The CMP (Fig. 9b) presents larger α-Al cells than the FMP (Fig. 9a). The HAZ (Fig. 9c) has a more disconnected Si-rich eutectic phase, even forming in some places isolated more or less rounded particles. Since the Si-rich network has fallen apart, there are no defined α-Al cells, hence cell size determination is not applicable.

A similar volume at the melt pool border was scanned for the 200°C build platform temperature material. Representative tomographies of the Si-rich phases of the three different melt pool zones can be observed in Fig. 9d,e,f. In this case the Si-rich precipitates are large enough to be properly detected in the SEM images used to build the tomography volume. The Si-rich eutectic network structure can be observed on the FMP (Fig. 9d) and the CMP (Fig. 9e), the connectivity appearing to be lower on the latter. In this case the α-Al cells are also, as expected, larger for the CMP. The HAZ seems to present very low connectivity of the Si-rich eutectic phase.

It should be noted that the FIB milling technique used in this research causes slight gallium (Ga) contamination of the sample [21]. This contamination is believed here to have a weak effect on the morphology of the phases observed by FIB/SEM, as also assumed in [22].

Only 3D microstructural characterisation is able to prove the high 3D connectivity of the Si-rich eutectic microstructure in the FMP zone. Table 3 provides the connectivity of the Si-rich eutectic phase in the different zones. Connectivity is defined as the volume occupied by the largest object divided by the total volume occupied by all the objects (here objects are the Si-rich eutectic) [23]. The concerned objects are those obtained after thresholding to keep only the Si-rich network of the microstructure. The connectivity of this network is found to be higher in the 35°C build platform material. It is also zone dependent. The CMP is slightly less connected than the FMP. The HAZ has a very low connectivity, the eutectic network having disintegrated in this region.

The thickness of the Si-rich network has been measured using the 3D characterisations but with the limitation that the resolution is of 5 nm. Table 3 provides these estimates based on a “sphere fitting” method using the Avizo and CTAn software [24]. In this approach, the structure thickness measurement process starts with a “skeletonisation” identifying the median axes of all structures. Once the median axis is calculated, the distance from the median axis to the local object surface is computed and the “sphere fitting” local thickness measurement is made for all the voxels lying along this axis. In that way the tested object can be characterised by a distribution of the measured thicknesses. In this study, the object thickness is defined based on the generated structure thickness histogram and corresponds to the maximum of the structure thickness distribution, i.e., the most frequent thickness. This is more adapted to these 3D observations and a better alternative to the mean value.

It is clear that the Si-rich network is finer in the 35°C samples compared to the 200°C ones. This is true in the FMP but also in the CMP and HAZ. The HAZ also presents larger particles (that can no longer really be called a network) than in the FMP. This is expected due to the microstructure growth occurring with the reheating of the zone of the previously melted layer that will correspond to the HAZ.

Fig. 10 shows a 3D rendering that clearly evidences that in the FMP and CMP the α-Al cells have a tubular shape. It can be linked to the grain orientation and fundamentally to local temperature gradients [25,26]. These cells can therefore be defined with two dimensions, diameter and length.

Table 4 presents the α-Al cell size in the FMP and CMP zones of the two materials characterised using 2D images. The HAZ cannot be considered to have a microstructure composed of a Si-rich eutectic network filled with α-Al cells, the network not being present and the α-Al phase not being constituted of well-defined cells. Note that the “2D length” of the cell is measured on some well oriented grains regarding the polished sample. This measurement method does however present some limitations if the cell is slightly inclined.

Table 5 presents the same characterisation but based on the 3D observations. This measurement also uses the “best fitting sphere” method already used for the thickness of the Si-rich network, but this time applied to the α-Al cells. Very similar values are found for the diameter of the cells when comparing Tables 4 and 5, confirming that this microstructure characteristic can be reliably determined in 2D, contrarily to the connectivity. Note that in 3D the length is not provided as it cannot be reliably determined with the present data. Indeed, the majority of the elongated cells are longer than the analysed thickness of the 3D volumes (see Fig. 10). In addition, the “sphere fitting” method is not appropriate for this characterisation.

The microstructure size difference between the 35°C and 200°C build platform temperature alloys is thus evidenced in Tables 4 and 5. All measured dimensions are larger for the 200°C case. In particular, the difference observed in diameter is much more significant, attaining a 78% increase in the FMP α-Al cell diameter (or 40% considering 3D data from Table 5). Regarding the two distinct zones, the α-Al dimensions of the CMP are logically larger than those of the FMP, although there is virtually no difference in length between FMP and CMP for the 35°C case. The main increase is found in the diameter for both cases.

### 3.3. Damage characterisation

In order to establish a link between the microstructure and the mechanical properties of the materials, SEM fractography and damage analyses of the tested tensile specimens were performed. The fracture surfaces of the 35°C and 200°C build platform temperature materials are shown in Fig. 11a,b, respectively. The typical size of the dimples is comparable to the cell size (Tables 4 and 5), confirming that damage is associated to the Si-rich network, as extensively discussed by Zhao et al. [8] for samples manufactured on the same equipment and with the same processing conditions (35°C samples).

Fig. 11c,d presents the microstructural damage of the 35°C and 200°C build platform materials at the vicinity of the fracture surface, along the longitudinal plane, at the mid-section of tensile testing specimens after failure. This surface observation confirms that damage initiates in the Si-rich network in both materials. The damage mechanism is then related to the fracture or the decohesion of the large Si phase present in this network. The areas of interest exemplified in Fig. 11c,d were analysed with the ImageJ software to determine the damage events on the different materials, distinguishing between the different melt pool zones. An indicator of damage nucleation is the surface density of cavities. The results are presented in Table 6. The 200°C build platform temperature material presents about 50% more damage events than the 35°C one. The FMP and CMP zones present a very similar damage level in both cases. However, the HAZ is significantly less damaged, the number of cavities being less than half of the ones in the other zones.

## 4. Discussion

The origin of the difference in mechanical behaviour of the 35°C and 200°C build platform temperature materials (Fig. 1) is undoubtedly multimodal, but there is certainly a relation with the microstructural differences.

### 4.1. Microstructural differences

Looking at the mesostructural level (Fig. 4), the melt pool borders of both materials appear to be quite different. The 200°C build platform temperature case presents a melt pool border twice as thick as the 35°C material. The thicknesses of the CMP and HAZ zones forming the melt pool border increase in extent in similar proportion when increasing the build platform temperature, both doubling in thickness. This variation is surely due to the larger heat input involved in the building process of the 200°C material. The melt pool border is kept at a higher temperature for a longer time, resulting in a lower cooling rate and consequently a more pronounced growth of the CMP and HAZ.

The HAZ is a zone where the Si-rich eutectic network is disintegrated. Combined with the CMP, which has a lower Si-rich eutectic phase connectivity than the FMP, they form the melt pool border, a zone that can be considered weaker than the FMP [27]. Indeed, the CMP contains a significantly less dense network, which gives strength to the material. In the case of the 200°C build platform temperature sample, the melt pool border zone is larger, it will experience more deformation and can potentially be a weakening factor.

The significance of the effect of the melt pool structure on the general mechanical behaviour will partly depend on the loading orientation. In the case of vertical loading, there can be a partition in strain between the zones. Thus, the weakest zone, the HAZ, is expected to undergo higher strain than the other two. The reported difference between horizontal and vertical mechanical properties [17,18] can thus be justified by the anisotropy of the melt pool structure. In the present study the mechanical testing was performed by loading in a horizontal direction with regards to the build platform. This means that the strain experienced by the three melt pool zones will be quite similar and the influence of strain localisation will not be as significant as is expected in the vertical orientation case [8].

Analysing the microstructure, it is clear that the one of the 35°C build platform case is finer. Due to the higher heat input and the lower temperature gradient, the α-Al cells, which can be characterised in both the FMP and CMP, are larger for the 200°C build platform material, which also contains a thicker Si-rich network (Table 3). The 200°C samples show clearly a lower connectivity. The Si-rich eutectic phase, of higher strength than the α-Al phase, performs the task of stress bearer, the α-Al yielding when stress is transferred to it [28].

The Si-rich precipitates inside the α-Al phase present such a small size in the 35°C build platform temperature material that they cannot be accurately captured via FIB/SEM 3D imaging to allow for a comparison with the ones detected in the 200°C build platform material. This fact is however indicative of a difference in size of these fine precipitates. They also tend to present needle-shapes when growing.

## 4.2. Strengthening mechanism

Fig. 1 clearly evidences a lower strength for the 200°C material compared to the 35°C case. The strengthening mechanism is thus analysed in the light of the characterised microstructure using simple analytical models of material strength.

The yield strength can be predicted as a contribution of the network and of the Al cells. In the cells, the strengthening is classically the sum of friction stress $\sigma_0$ and various additional strengthening effects (precipitates, dislocations, solid solution and eutectic network boundaries). As for the network, its load bearing capacity $\sigma_{\text{load}}$ can be inferred from [28] to be about 380 MPa at the yield point of the LPBF AlSi10Mg sample. Li et al. [15] and Canelo-Yubero et al. [29] suggested to simply combine these two contributions using an isostrain rule of mixture, expressed as

$$\sigma_y = f_{\text{cell}} \times \left(\sigma_0 + \Delta\sigma_{\text{preci}} + \Delta\sigma_{\text{bound}} + \Delta\sigma_{\text{ss}} + \Delta\sigma_{\text{disloc}}\right) + f_{\text{net}} \times \sigma_{\text{load}} \qquad (1)$$

$\Delta\sigma_{\text{preci}}$ represents the strengthening contribution from the Si precipitates in the Al cells via the Orowan mechanism,

$$\Delta\sigma_{\text{preci}} = \frac{MGb}{l} \qquad (2)$$

where $l$ is the particle spacing in the glide plane, which can be calculated with the diameter $d_{\text{preci}}$ and the volume fraction $f_v$ of the particles.

$$l = \frac{d_{\text{preci}}}{2}\sqrt{\frac{2\pi}{3f_v}} \qquad (3)$$

$\Delta\sigma_{\text{bound}}$ is the contribution of the boundary of the Si-rich eutectic network impeding dislocation motion [25], which can be analogous to the Hall-Petch effect.

$$\Delta\sigma_{\text{bound}} = \frac{k_d}{\sqrt{d_{\text{net}}}} \tag{4}$$

where $d_{\text{net}}$ denotes the width of the Si-rich eutectic network, which is taken as the α-Al cell diameter value extracted from the 3D FIB/SEM characterisation (Table 5).

$\Delta\sigma_{\text{ss}}$ represents the strengthening effect of the solid solution of Si in the α-Al matrix

$$\Delta\sigma_{\text{ss}} = k_{(\text{Si})}(C_{\text{Si}})^{2/3} \tag{5}$$

where $k_{(\text{Si})}$ is a constant and $C_{\text{Si}}$ is the concentration of Si in solid solution.

$\Delta\sigma_{\text{disloc}}$ denotes the strengthening effect from the initial dislocation forest

$$\Delta\sigma_{\text{disloc}} = \alpha M G b \sqrt{\rho_d} \tag{6}$$

where $\alpha$ is a material constant and $\rho_d$ is the initial dislocation density in the material.

$f_{\text{cell}}$ and $f_{\text{net}}$ denote the volume fraction of the α-Al cells and the Si-rich eutectic network, respectively. Note that $f_{\text{cell}} + f_{\text{net}} \approx 1$.

The values of the above mentioned parameters are given in Table 7. The last column of this table details the origin of these parameters. They correspond for each build platform temperature to the microstructure of the FMP zone, which predominates in the material. A discussion of this selection is provided in the supplementary material section. Note that to determine the equivalent diameter of the Si precipitates TEM data were used for the 35°C build platform temperature case [8] and FIB/SEM tomography data for the 200°C build platform temperature material. Indeed, the 5 nm resolution of the FIB/SEM tomographies is not high enough to characterise the fine Si precipitates in the 35°C case.

The calculated strengthening components and the corresponding yield strength are presented in Table 8. It should be noted that the strengthening effect of the $Mg_2Si$ precipitates was found to be quite low [38] and was therefore disregarded in the present work.

The prediction overestimates the yield strength for both materials. This was expected since only the FMP zone, i.e., the strongest part of the material, is considered. In addition, some parameters are estimated based on literature but could not be measured with precision in our particular case. Nevertheless, the calculations with these classical strengthening models capture the experimental microstructure-strength correlation. With the use of this prediction, it is found that the main contribution to the strength originates from the fine Si precipitates for the 35°C material, which is coherent with the proposition of Takata et al. [39]; $\Delta\sigma_{\text{preci}}$ is also responsible for the higher strength compared with the 200°C material. Indeed, Figs. 6 and 8 clearly show that the 200°C material presents much larger Si-rich precipitates than the 35°C alloy; the precipitate strengthening has been shown to significantly drop in relation to the size increase of the precipitates [31]. The importance of the cell size is also reflected on the Si-rich eutectic network boundary contribution to strength through dislocation motion hindering.

Another aspect that will affect mechanical behaviour is the separation degree of the material state from equilibrium. The 200°C built platform temperature alloy is closer to equilibrium and, as a result, the α-Al matrix is expected to have less Si in solid solution. As shown in Table 8 this fact results in a lower strength in the 200°C case. It has to be noted that, in absence of more accurate data and for illustrative purposes, a value of 1.6 wt. % Si in solid solution was used for the calculations in the 200°C build platform temperature case [33]. Indeed, the Si concentration in solid solution will be lower for the 200°C material compared to the 2.4 wt. % of the 35°C case [8] since it will be closer to equilibrium, but the used value of 1.6 wt. % should be regarded as a lower bound, the real concentration is expected to be slightly higher.

Only the dislocation strengthening component contributes to reducing the difference between the 35°C and 200°C build platform temperature materials, since it is higher for the latter.

### 4.3. Damage and ductility

The damage characterisation was performed taking into account the different melt pool zones. The results shown in Table 6 indicate that 55% more damage sites are evidenced in the 200°C build platform temperature material, which will compromise the ductility of the material. This larger amount of damage nucleation can be associated to the thicker Si-rich network in the case of the 200°C material (Table 3). Indeed, larger second phases are expected to present a higher fracture probability [40,41]. This has been statistically evidenced by Hannard et al. [41] on 6xxx series aluminium alloys containing different sizes of Fe-rich second phases.

As already discussed for the strengthening in the preceding section, these materials are composed of a rigid and brittle Si-rich backbone (the eutectic), the cells of which are filled with ductile aluminium. In such a microstructure, for a given overall strain in the composite, the rigid backbone is likely to exhibit a similar strain in both 35°C and 200°C materials. It thus results that the network with larger particles (200°C) exhibits more damage nucleation. This should lead to an earlier fracture of this material, but it is compensated by the following two effects justifying the similar fracture strain of both materials:

- The lower stress, retarding void growth;

- The larger distance between two microcracks in the 200°C material due to larger ductile α-Al cells (delaying coalescence).

In the LPBF AlSi10Mg materials the situation is a bit more complex than for the simple globular-shaped second phase particle materials studied by Hannard et al. [41]. Here the second phase is also highly interconnected in the FMP. A less connected second phase is expected to accommodate more plastic deformation before failure [42]. This is probably what is evidenced in the HAZ of both materials where limited damage is manifest (Table 6). The HAZ is also softer since the fragmented Si-rich network bears lower stress according to the shear lag theory [43], which may also impact damage nucleation.

Fracture strain could also be affected by the initial porosity. The 35°C build platform temperature material has a higher initial porosity level. It was measured on similar samples built with the same machine and found to be 0.039% in the 35°C material and 0.016% in the 200°C material [9]. This porosity level difference, coupled with the higher stress level, could also favour earlier damage coalescence, limiting the fracture strain of the 35°C material. However, Zhao et al. [8] have demonstrated the dominant effect of the Si-rich network structure on the damage process under static loading. Porosity is thus expected to play a second order role in the fracture strain difference evidenced in Fig. 1. Nevertheless, the large initial porosity dominates the fracture mechanism under fatigue loading [16].

Distinguishing between the different zones, damage is similar for the FMP and CMP zones and lower for the HAZ. As previously mentioned, taking into account the loading direction in the tensile tests (horizontal), it has to be noted that the strain experienced by the three zones can be considered similar. In this case, the weaker melt pool border will be able to accommodate the limited strain better than the stronger FMP, dominated by the more damage-prone interconnected Si-rich eutectic network. As a consequence, there is no zone that is predominantly acting as the weakest link for failure. If the loading direction was vertical, it could be expected that the melt pool border would experience more strain and could act more clearly as a critical zone. A future work is needed to address this issue.

## 5. Conclusions

The strength of the SLM AlSi10Mg decreases significantly with a build platform temperature increase from 35°C to 200°C, while the fracture strain is scarcely affected. This can be attributed to the following finer scale microstructural differences that have been thoroughly characterised in the present study:

- The 35°C build platform temperature case features a melt pool border of half the thickness of the 200°C counterpart. The latter presents both a coarse melt pool (CMP) and a heat affected zone (HAZ) twice as thick.

- The grain size, morphology and texture are little affected by the change in build platform temperature.

- The build platform temperature has a decisive impact on the fine cellular microstructure of the material. The fine precipitates inside the α-Al cells are five times larger in the 200°C build platform temperature case. The tubular cellular microstructure of the materials has been revealed by a 3D FIB/SEM analysis. The cell size and eutectic phase thickness are also increased with the build platform temperature increment.

-The Si-rich network is slightly more connected in the fine melt pool (FMP) of the 35°C material compared to the 200°C and clearly more connected than in the HAZ

Concerning strength, the AlSi10Mg built with a platform at 35°C presents a yield strength 83 MPa larger than when built at 200°C. An analytical model exploiting the microstructure observations has revealed the significant contribution of the fine Si-rich precipitates inside the α-Al cells to the material strength. This strengthening is further enhanced in the 35°C material compared to the 200°C case by the cell diameter difference, being 1.8 times larger for the latter.

Regarding ductility, the fracture strain is similar in both cases. The 200°C material presents however 55% more damage sites below the fracture surface at fracture strain, so it is clearly more damage tolerant. Void growth is slowed down and coalescence is delayed in this 200°C microstructure due to the lower strength and larger α-Al cells. The network connectivity may also play a role in damage initiation, thus justifying the lower damage level in the HAZ.

## Acknowledgements

The authors acknowledge the support of Laurence Ryelandt (UCLouvain) and Joël Lachambre (Université de Lyon). JGSM acknowledges the support of the Fonds de la recherche scientifique - FNRS (FRIA grant), Belgium. This research has also been funded (from January 2017) by the European Research Council (ERC) under the European Union’s Horizon 2020 research and innovation program (grant agreement n°716678). This research work has also been supported from January 2019 by the WALInnov LongLifeAM project, Convention n°1810016, funded by the Service public de Wallonie Économie Emploi Recherche (SPW-EER). The access to the Zeiss NVision40 FIB/SEM was provided by the CLyM (Consortium Lyon Saint-Etienne de Microscopie) supported by the CNRS, the “GrandLyon” and the Rhône-Alpes Region (France).

## References

[1] N.T. Aboulkhair, M. Simonelli, L. Parry, I. Ashcroft, C. Tuck, R. Hague, 3D printing of aluminium alloys: additive manufacturing of aluminium alloys using selective laser melting, Prog. Mater. Sci. 106 (2019) 100578.
[2] T. Yu, H. Hyer, Y. Sohn, Y. Bai, D. Wu, Structure-property relationship in high strength and lightweight AlSi10Mg microlattices fabricated by selective laser melting, Mater. Des. 182 (2019) 108062.
[3] L. Wang, X. Jiang, M. Guo, X. Zhu, B. Yan, Characterisation of structural properties for AlSi10Mg alloys fabricated by selective laser melting, Mater. Sci. Technol. 33(18) (2017) 2274-2282.
[4] S. Romano, A. Brandão, J. Gumpinger, M. Gschweitl, S. Beretta, Qualification of AM parts: Extreme value statistics applied to tomographic measurements, Mater. Des. 131 (2017) 32-48.
[5] Z. Li, Y. Nie, B. Liu, Z. Kuai, M. Zhao, F. Liu, Mechanical properties of AlSi10Mg lattice structures fabricated by selective laser melting, Mater. Des. 192 (2020) 108709.
[6] N.D. Parab, L. Xiong, Q. Guo, Z. Guo, C. Kirk, Y. Nie, X. Xiao, F. Kamel, W. Everheart, W.W. Chen, L. Chen, T. Sun, Investigation of dynamic fracture behavior of additively manufactured Al-10Si-Mg using high-speed synchrotron X-ray imaging, Addit. Manuf. 30 (2019) 100878.
[7] K.G. Prashanth, S. Cudino, T. Maity, J. Das, J. Eckert, Is the energy density a reliable parameter for materials synthesis by selective laser melting?, Mater. Res. Lett. 5 (2017) 386-390.
[8] L. Zhao, J.G. Santos Macías, L. Ding, H. Idrissi, A. Simar, Damage mechanisms in selective laser melted AlSi10Mg under as built and different post-treatment conditions, Mater. Sci. Eng. A 764 (2019) 138210.
[9] L. Zhao, J.G. Santos Macías, A. Dolimont, A. Simar, E. Rivière-Lorphèvre, Comparison of residual stresses obtained by the crack compliance method for parts produced by different metal additive manufacturing techniques and after friction stir processing, Addit. Manuf. 36 (2020) 101499.
[10] M. Awd, S. Siddique, J. Johannsen, C. Emmelmann, F. Walther, Very high-cycle fatigue properties and microstructural damage mechanisms of selective laser melted AlSi10Mg alloy, Int. J. Fatigue 124 (2019) 55-69.

[11] D. Buchbinder, W. Meiners, K. Wissenbach, R. Poprawe, Selective laser melting of aluminum die-cast alloy─Correlations between process parameters, solidification conditions, and resulting mechanical properties, J. Laser Appl. 27 (2015) S29205.
[12] D. Kim, J. Hwang, E. Kim, Y. Heo, W. Woo, S. Choi, Evaluation of the stress-strain relationship of constituent phases in AlSi10Mg alloy produced by selective laser melting using crystal plasticity FEM, J. Alloy. Compd. 714 (2017) 687-697.
[13] X. Liu, C. Zhao, X. Zhou, Z. Shen, W. Liu, Microstructure of selective laser melted AlSi10Mg alloy, Mater. Des. 168 (2019) 107677.
[14] L. Thijs, K. Kempen, J.P. Kruth, J. Van Humbeeck, Fine-structured aluminium products with controllable texture by selective laser melting of pre-alloyed AlSi10Mg powder, Acta Mater. 61 (2013) 1809-1819.
[15] Z. Li, Z. Li, Z. Tan, D. Xiong, Q. Guo, Stress relaxation and the cellular structure dependence of plastic deformation in additively manufactured AlSi10Mg alloys, Int. J. Plast. 127 (2020) 102640.
[16] J.G. Santos Macías, C. Elangeswaran, L. Zhao, B. Van Hooreweder, J. Adrien, E. Maire, J.-Y. Buffière, W. Ludwig, P.J. Jacques, A. Simar, Ductilisation and fatigue life enhancement of selective laser melted AlSi10Mg by friction stir processing, Scr. Mater. 170 (2019) 124-128.
[17] EOS GmbH - Electro Optical Systems, Material Data Sheet for AlSi10Mg processed at a build platform temperature of 35°C for EOS M 290. München 2014.
[18] EOS GmbH - Electro Optical Systems, Material Data Sheet for AlSi10Mg processed at a build platform temperature of 200°C for EOS M 280. München 2013.
[19] A. Squillace, U. Prisco, Influence of filler material on micro- and macro-mechanical behaviour of laser-beam-welded T-joint for aerospace applications, Proc. Inst. Mech. Eng. Part L J. Mater. Des. Appl. 223(3) (2009) 103-115.
[20] Y.J. Liu, Z. Liu, Y. Jiang, G.W. Wang, Y. Yang, L.C. Zhang, Gradient in microstructure and mechanical property of selective laser melted AlSi10Mg, J. Alloy. Compd. 735 (2018) 1414-1421.
[21] K.A. Unocic, M.J. Mills, G.S. Daehn, Effect of gallium focused ion beam milling on preparation of aluminium thin foils, J. Microsc. 240 3 (2010) 227-238.
[22] F. Lasagni, A. Lasagni, E. Marks, C. Holzapfel, F. Mücklich, H.P. Degischer, Three-dimensional characterization of ‘as-cast’ and solution-treated AlSi12(Sr) alloys by high-resolution FIB tomography, Acta Mater. 55 11 (2007) 3875-3882.
[23] A. Asghar, G. Requena, E. Boller, Three-dimensional rigid multiphase networks providing high-temperature strength to cast AlSi10Cu5Ni1-2 piston alloys, Acta Mater. 59 (2011) 6420-6432.
[24] G. Pyka, G. Kerckhofs, J. Schrooten, M. Wevers, The effect of spatial micro-CT image resolution and surface complexity on the morphological 3D analysis of open porous structures, Mater. Charact. 87 (2014) 104-115.
[25] J. Wu, X.Q. Wang, W. Wang, M.M. Attallah, M.H. Loretto, Microstructure and strength of selectively laser melted AlSi10Mg, Acta Mater. 117 (2016) 311-320.
[26] Z.H. Xiong, S.L. Liu, S.F. Li, Y. Shi, Y.F. Yang, R.D.K. Misra, Role of melt pool boundary condition in determining the mechanical properties of selective laser melting AlSi10Mg alloy, Mater. Sci. Eng. A 740-1 (2019) 148-156.
[27] J. Delahaye, J. Tchoufang Tchuindjang, J. Lecomte-Beckers, O. Rigo, A.M. Habraken, A. Mertens, Influence of Si precipitates on fracture mechanisms of AlSi10Mg parts processed by selective laser melting, Acta Mater. 175 (2019) 160-170.

[28] D. Kim, W. Woo, J. Hwang, K. An, S. Choi, Stress partitioning behavior of an AlSi10Mg alloy produced by selective laser melting during tensile deformation using in situ neutron diffraction, J. Alloy. Compd. 686 (2016) 281-286.

[29] D. Canelo-Yubero, C. Etzlstorfer, R. Koos, H. Germann, T. Steffens, A. Stark, E. Boller, G. Requena, Load partition during hot deformation of AlSi12 and AlSi10Cu6Ni2 alloys: a quantitative evaluation of the stiffness of Si networks, J. Mater. Sci. 55 (2020) 14558-14570.

[30] O.R. Myhr, O. Grong, H.G. Fjaer, C.D. Marioara, Modelling of the microstructure and strength evolution in Al-Mg-Si alloys during multistage thermal processing, Acta Mater. 52 (2004) 4997-5008.

[31] A. Simar, Y. Bréchet, B. De Meester, A. Denquin, T. Pardoen, Sequential modeling of local precipitation, strength and strain hardening in friction stir welds of an aluminum alloy 6005A-T6, Acta Mater. 55 (2007) 6133-6143.

[32] N. Hansen, Hall-Petch relation and boundary strengthening, Scr. Mater. 51 (2004) 801-806.

[33] X.P. Li, X.J. Wang, M. Saunders, A. Suvorova, L.C. Zhang, Y.J. Liu, M.H. Fang, Z.H. Huang, T.B. Sercombe, A Laser Powder Bed Fusion and solution heat treatment refined Al-12Si alloy with a controllable ultrafine eutectic microstructure and 25% tensile ductility, Acta Mater. 95 (2015) 74-82.

[34] T. Huang, L. Shuai, A. Wakeel, G. Wu, N. Hansen, X. Huang, Strengthening mechanisms and Hall-Petch stress of ultrafine grained Al-0.3%Cu, Acta Mater. 156 (2018) 369-378.

[35] A. Hadadzadeh, B.S. Amirkhiz, J. Li, A. Odeshi, M. Mohammadi, Deformation mechanism during dynamic loading of an additively manufactured AlSi10Mg_200C, Mater. Sci. Eng. A 722 (2018) 263-268.

[36] N. Takata, H. Kodaira, K. Sekizawa, A. Suzuki, M. Kobashi, Change in microstructure of selectively laser melted AlSi10Mg alloy with heat treatments, Mater. Sci. Eng. A 704 (2017) 218-228.

[37] M. Tang, P.C. Pistorius, Anisotropic mechanical behavior of AlSi10Mg parts produced by Laser Powder Bed Fusion, JOM 69 (2017) 516-522.

[38] A. Hadadzadeh, B.S. Amirkhiz, M. Mohammadi, Contribution of $Mg_2Si$ precipitates to the strength of direct metal laser sintered AlSi10Mg, Mater. Sci. Eng. A 739 (2019) 295-300.

[39] N. Takata, M. Liu, H. Kodaira, A. Suzuki, M. Kobashi, Anomalous strengthening by supersaturated solid solutions of selectively laser melted Al-Si-based alloys, Addit. Manuf. 33 (2020) 101152.

[40] G. Huber, Y. Brechet, T. Pardoen, Predictive model for void nucleation and void growth controlled ductility in quasi-eutectic cast aluminium alloys, Acta Mater. 53 9 (2005) 2739-2749.

[41] F. Hannard, A. Simar, E. Maire, T. Pardoen, Quantitative assessment of the impact of second phase particle arrangement on damage and fracture anisotropy, Acta Mater. 148 (2018) 456-466.

[42] K. Bugelnig, F. Sket, H. Germann, T. Steffens, R. Koos, F. Wilde, E. Boller, G. Requena, Influence of 3D connectivity of rigid phases on damage evolution during tensile deformation of an AlSi12Cu4Ni2 piston alloy, Mater. Sci. Eng. A 709 (2018) 193-202.

[43] V.C. Nardone, K.M. Prewo, On the strength of discontinuous silicon carbide reinforced aluminum composites, Scr. Metall. 20 (1986) 43-48.

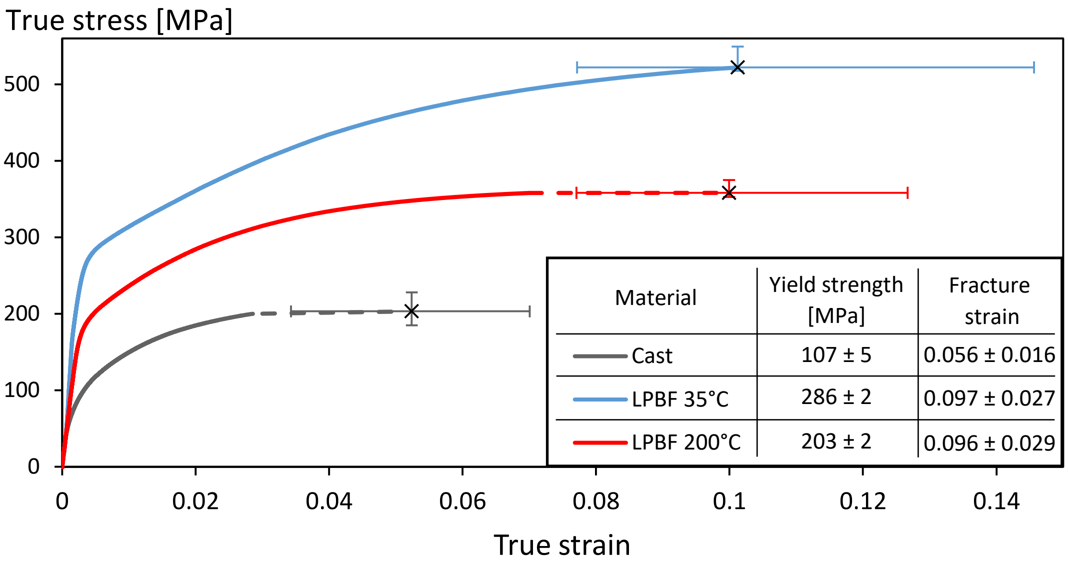

**Fig. 1.** Representative tensile true stress - true strain curves of AlSi10Mg produced by casting or LPBF with a build platform temperature of 35°C or 200°C. The last point of the curve is obtained from the force ($F_f$) at failure and the sample area ($A_f$) at failure ($\sigma_f = F_f/A_f$; $\varepsilon_f = \ln(A_0/A_f)$). The error bars correspond to the lowest and highest stresses and strains at failure of the tested samples. A linear extrapolation links the end of the true stress - true strain curve to the failure point to show the post-necking behaviour. The inset table provides mean associated values with a 99% confidence interval.

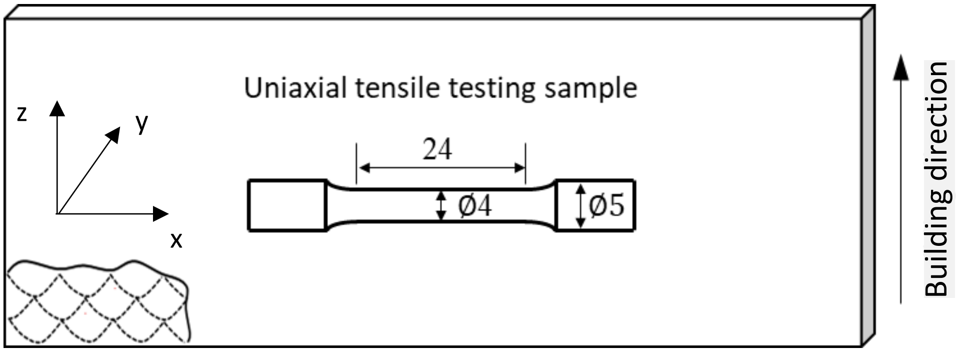

**Fig. 2.** Schematic representation of LPBF AlSi10Mg plates showing the orientation of the melt pools and the mechanical testing specimens.

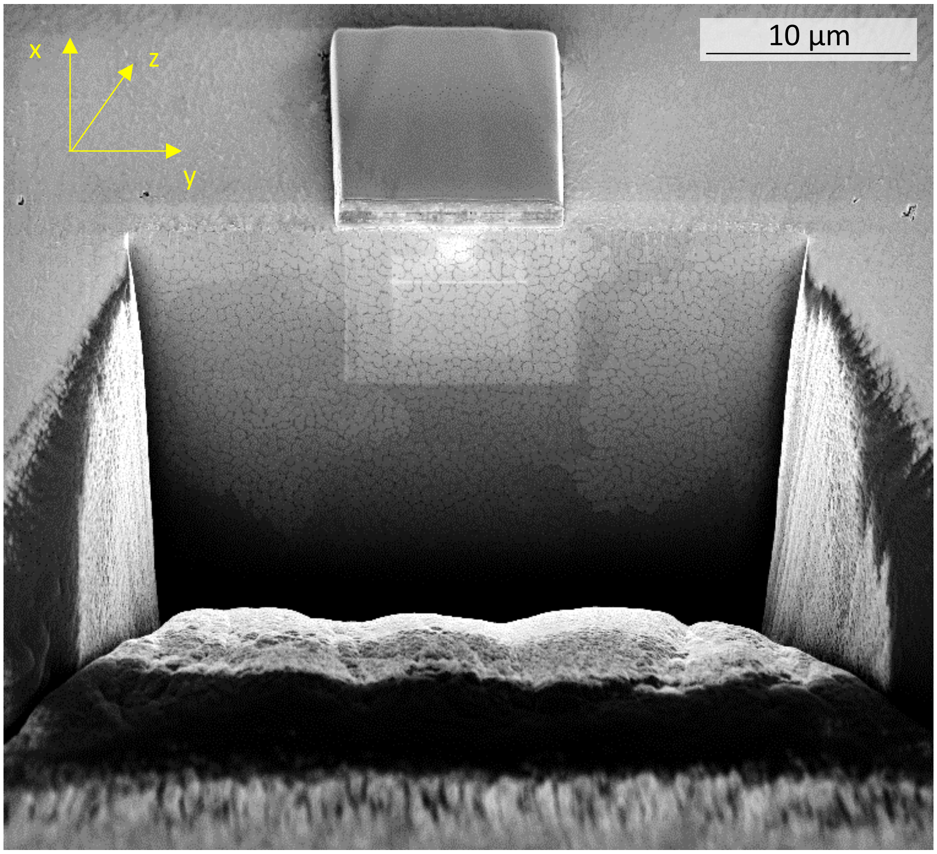

**Fig. 3.** Sample prepared for FIB/SEM tomography. The imprinted electron beam induced wolfram deposition into an ion beam induced carbon coating can be observed on the top of the figure. The trench at the front of the figure is created by removing material by FIB to expose the surface that will be the section of the FIB/SEM tomography volume. The sample x, y, z orientation axis is in reference to Fig. 2.

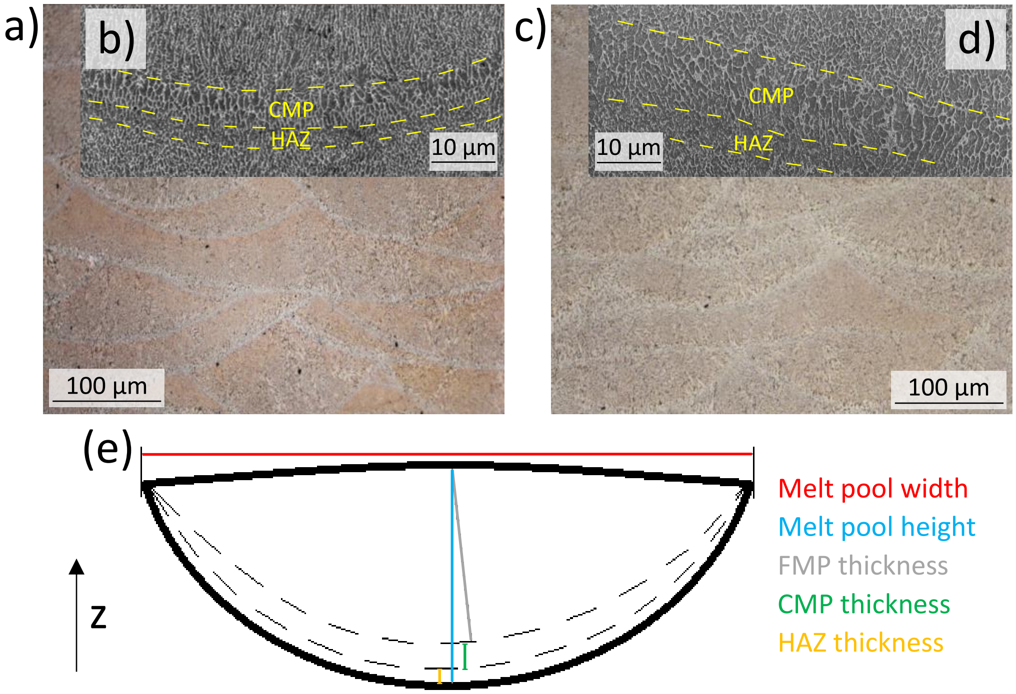

**Fig. 4.** OM micrographs and SEM insets of LPBF AlSi10Mg with build platform temperature of 35°C (a,b) and 200°C (c,d); e: Melt pool scheme featuring the three melt pool zones (FMP, CMP and HAZ) and the methodology by which dimensions are measured (width and height of the melt pool and thickness of the zones; see colour code).

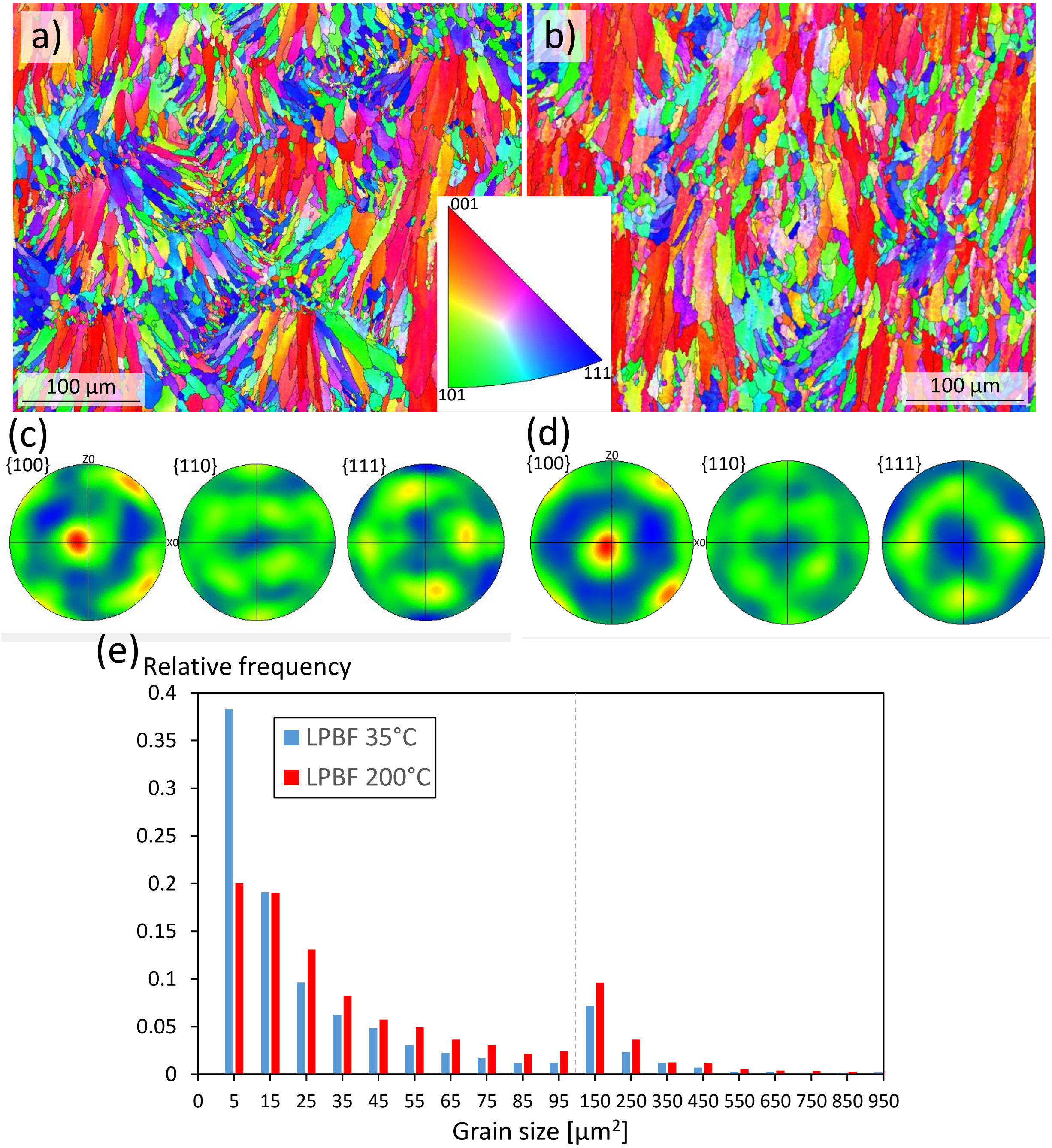

**Fig. 5.** EBSD map displayed in inverse pole figure colouring (a,b) and pole figures (c,d) of LPBF AlSi10Mg with build platform temperature of 35°C (a,c) and 200°C (b,d), showing predominant <100> orientation of the elongated grain structure along the building direction. The grain size (grain area) distribution is provided in (e) for both materials.

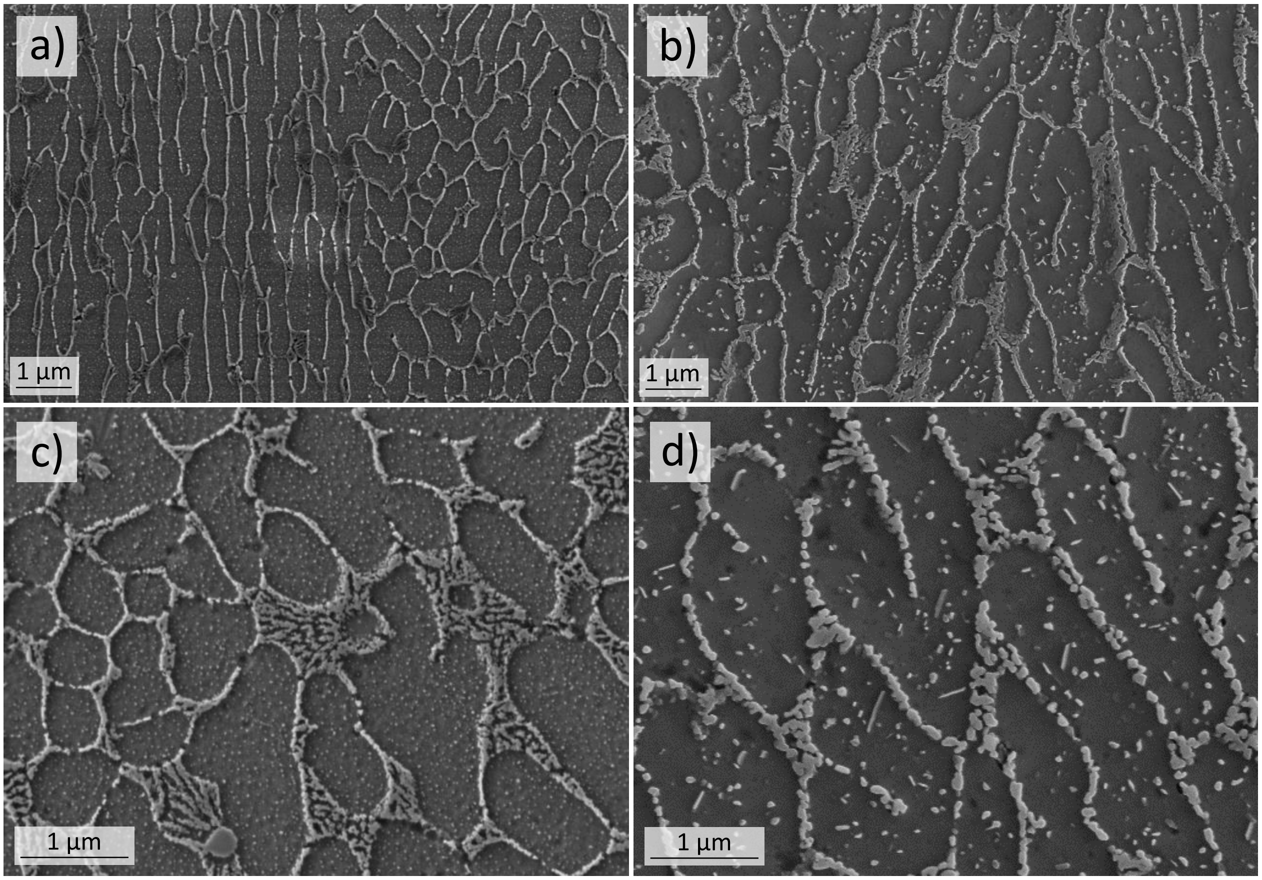

**Fig. 6.** SEM micrographs of the FMP zone of LPBF AlSi10Mg with build platform temperature of 35°C (a,c) and 200°C (b,d).

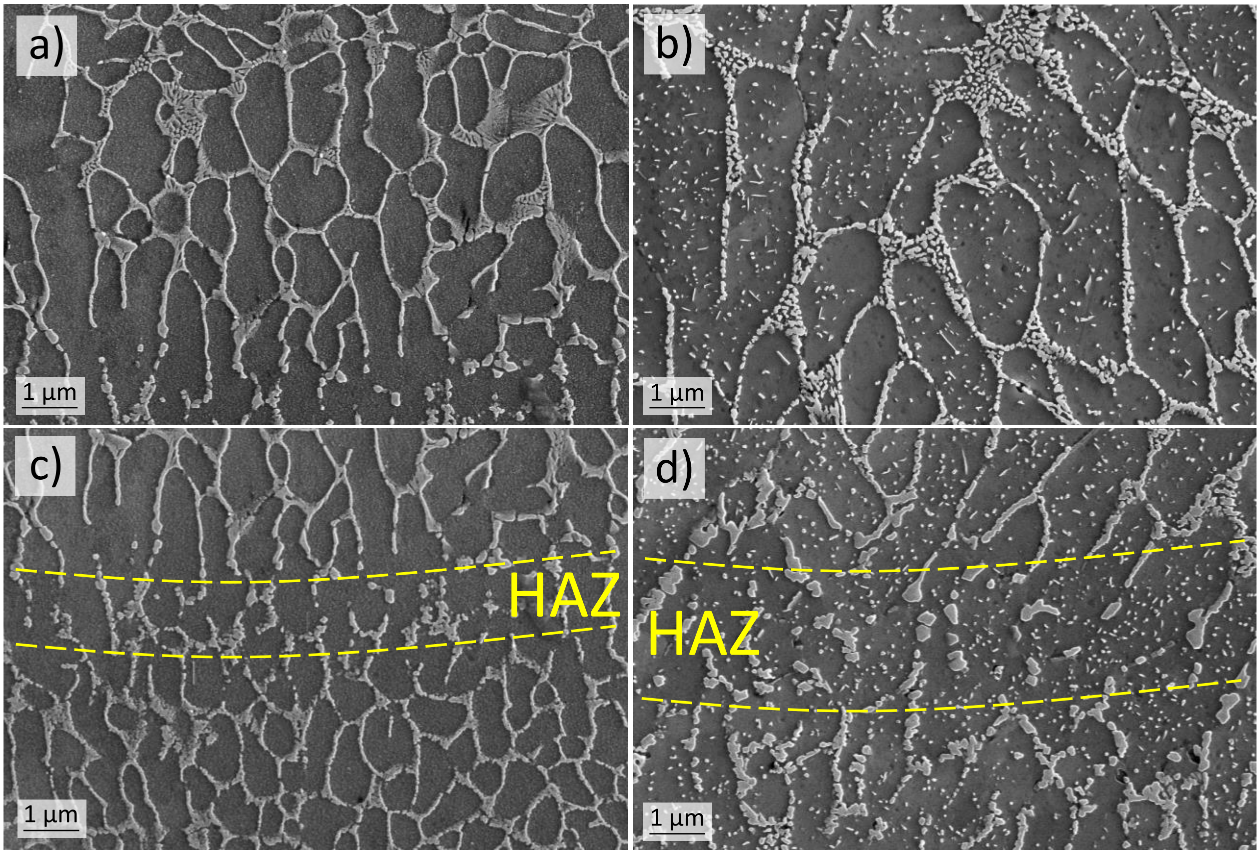

**Fig. 7.** SEM micrographs of the CMP zone of LPBF AlSi10Mg with build platform temperature of 35°C (a) and 200°C (b) and of the HAZ zone (in between the two yellow dashed lines) with build platform temperature of 35°C (c) and 200°C (d).

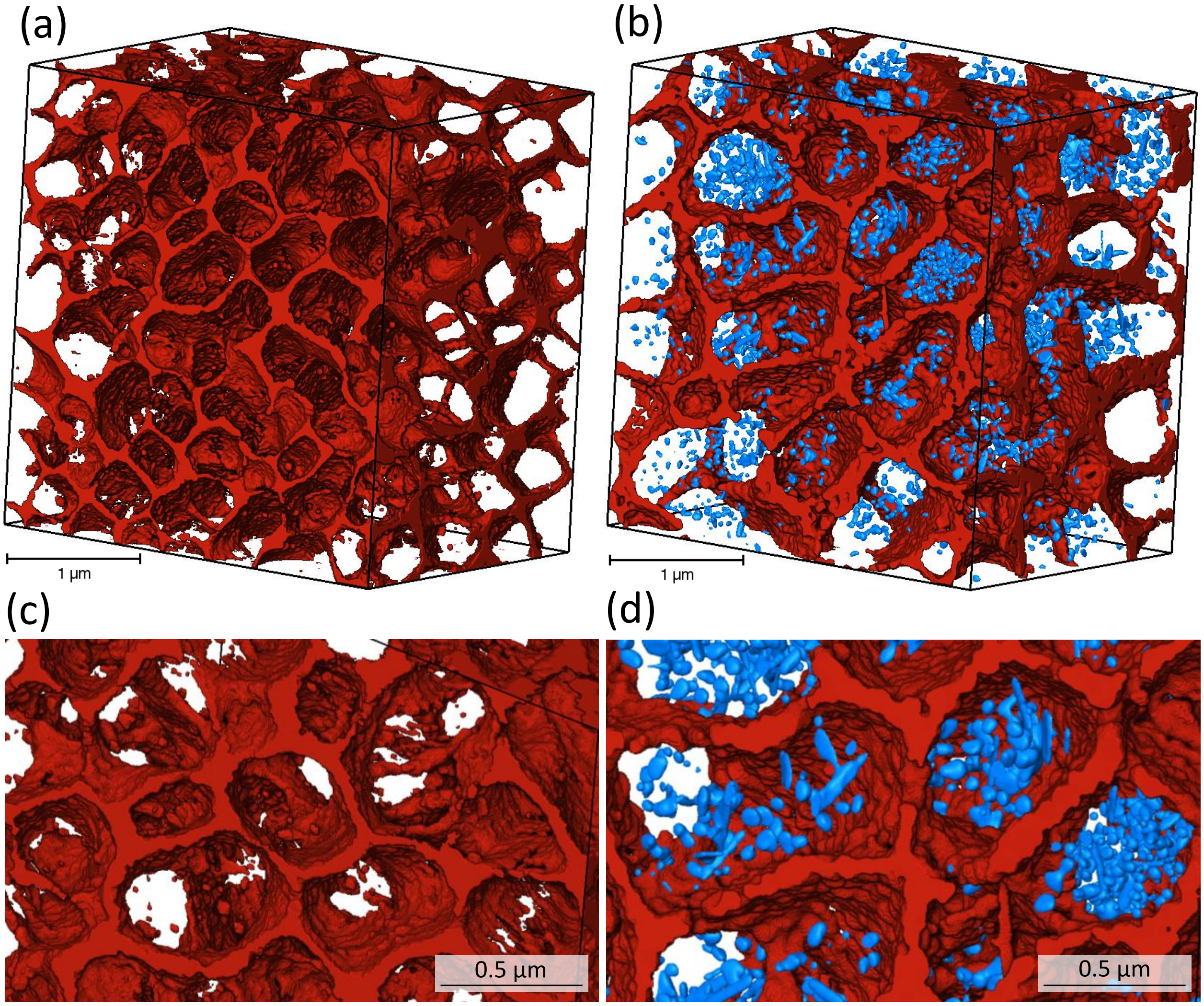

**Fig. 8.** FIB/SEM tomographies (3.5x3.4x2.5 µm) of Si-rich phases of FMP zone of LPBF AlSi10Mg with building platform temperature of 35°C (a) and 200°C (b) and respective zoomed regions for detail (c,d). The fine Si-rich precipitates inside the Al matrix can be identified only with the build platform temperature of 200°C and are highlighted in blue for better visibility.

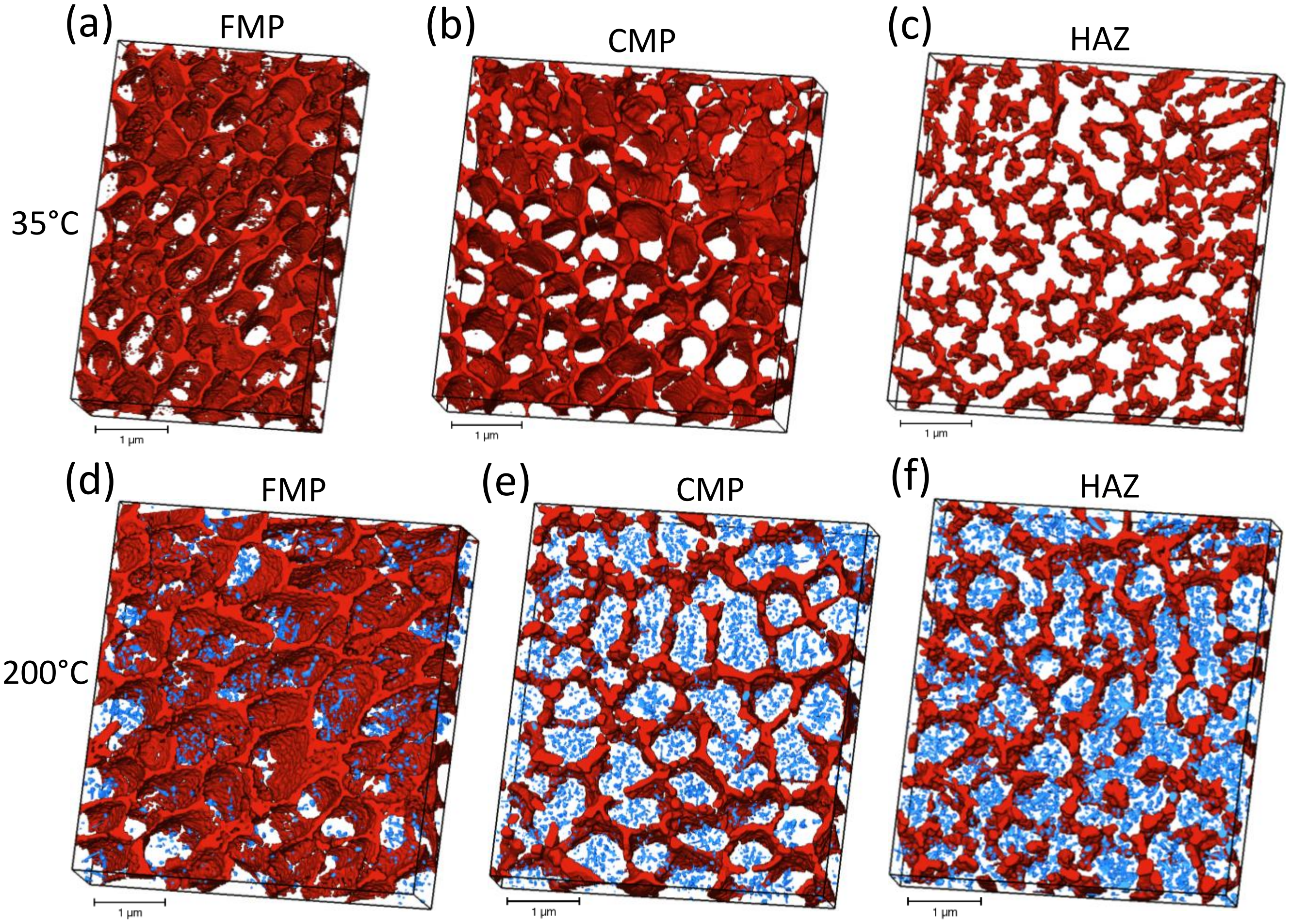

**Fig. 9.** FIB/SEM tomographies of Si-rich eutectic network of FMP (a), CMP (b) and HAZ (c) of LPBF AlSi10Mg with build platform temperature of 35°C and of Si-rich phases of FMP (d), CMP (e) and HAZ (f) of LPBF AlSi10Mg with build platform temperature of 200°C. Dimensions are, respectively, 5x3.4x1 µm, 5x5x1.7 µm, 5x5x0.5 µm, 5.3x5x1 µm, 5.3x4.7x0.7 µm and 5.3x4.7x0.7 µm. The fine Si-rich precipitates inside the Al matrix can be identified only with the build platform temperature of 200°C and are highlighted in blue for better visibility.

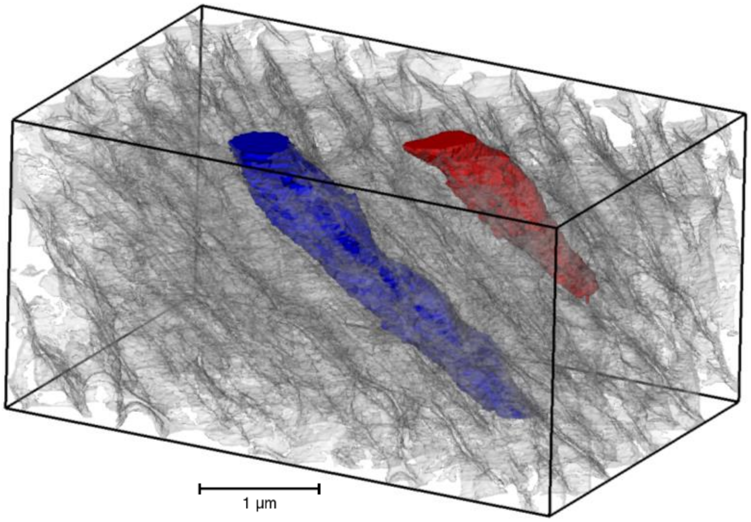

**Fig. 10.** FIB/SEM tomography of two long tubular cellular structures exiting the reconstructed volume of the 35°C material.

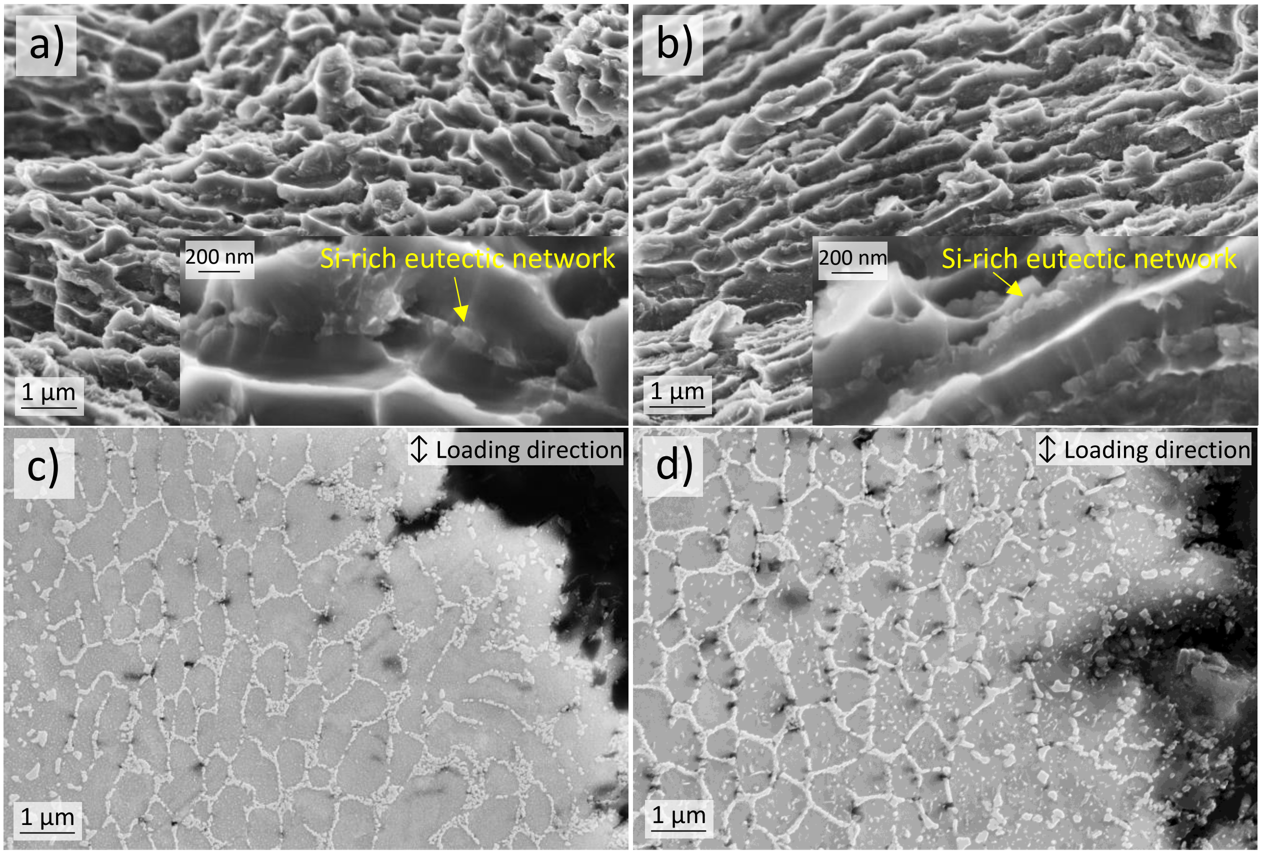

**Fig. 11.** SEM images of the fracture surfaces (a,b) and of polished surfaces under the fracture surface (c,d) for the LPBF AlSi10Mg samples with build platform temperature of 35°C (a,c) and 200°C (b,d).

**Table 1**. Chemical composition (wt. %) determined by ICP OES.

| Sample | Al | Si | Mg | Fe |
|---|---|---|---|---|
| **Cast** | 90.0 | 9.3 | 0.29 | 0.08 |
| **LPBF 35°C** | 89.6 | 9.7 | 0.40 | 0.12 |
| **LPBF 200°C** | 89.4 | 9.7 | 0.41 | 0.20 |

**Table 2**. Melt pool structure dimensions.

| $T_{Build\ platform}$ | Melt pool width | Melt pool height | FMP thickness | CMP thickness | HAZ thickness |
|---|---|---|---|---|---|
| **35°C** | 176 ± 13 µm | 60 ± 6 µm | 53 µm | 5.5 µm | 1.5 µm |
| **200°C** | 180 ± 13 µm | 64 ± 8 µm | 52 µm | 9 µm | 3 µm |

**Table 3**. Si-rich eutectic phase connectivity and thickness in LPBF AlSi10Mg.

| $T_{Build\ platform}$ and zone | Connectivity | Si-rich eutectic phase thickness |
|---|---|---|
| **35°C FMP** | 0.99 | 0.05 µm |
| **35°C CMP** | 0.85 | 0.07 µm |
| **35°C HAZ** | 0.10 | 0.09 µm |
| **200°C FMP** | 0.90 | 0.07 µm |
| **200°C CMP** | 0.80 | 0.10 µm |
| **200°C HAZ** | 0.20 | 0.10 µm |

**Table 4**. α-Al cell size measured on 2D SEM images.

| $T_{Build\ platform}$ | FMP α-Al diameter | FMP α-Al length | CMP α-Al diameter | CMP α-Al length |
|---|---|---|---|---|
| **35°C** | 0.32 ± 0.06 µm | 1.66 ± 0.36 µm | 0.53 ± 0.06 µm | 1.65 ± 0.26 µm |
| **200°C** | 0.57 ± 0.08 µm | 1.74 ± 0.39 µm | 0.85 ± 0.19 µm | 2.47 ± 0.59 µm |

**Table 5**. α-Al cell size measured on 3D FIB/SEM images.

| $T_{Build\ platform}$ | FMP α-Al diameter | CMP α-Al diameter |
|---|---|---|
| **35°C** | 0.37 µm | 0.50 µm |
| **200°C** | 0.52 µm | 0.70 µm |

**Table 6**. Number of cavities per µm$^2$ for the different melt pool zones of the LPBF AlSi10Mg material fabricated with a build platform temperature of 35°C and 200°C.

| $T_{Build\ platform}$ | Melt pool zone | | |
|---|---|---|---|
| | FMP | CMP | HAZ |
| **35°C** | 0.80 | 0.83 | 0.37 |
| **200°C** | 1.25 | 1.26 | 0.57 |

**Table 7**. Parameters used in Eqs. (1)-(6). The parameter selection is further discussed in the supplementary material section.

| **Parameter** | **Description** | **Unit** | **Values for 35°C / 200°C materials** | **Reference** |
|---|---|---|---|---|
| $\sigma_0$ | Friction stress | MPa | 10 | [30] |
| $M$ | Taylor factor | - | 2 | Textured alloy [31] |
| $G$ | Shear modulus | GPa | 27 | [30] |
| $b$ | Amplitude of Burger's vector | nm | 0.284 | [30] |
| $d_{\mathrm{preci}}$ | Equivalent diameter of Si precipitates | nm | 12/60 | Same sample TEM [8]/FIB/SEM in the present work |
| $f_v$ | Volume fraction of Si precipitates | % | 0.8/1.6 | Same sample TEM [8]/FIB/SEM in the present work (Fig. 8) |
| $k_d$ | Constant of Hall-Petch relation for aluminium | MPa· $\mathrm{m}^{1/2}$ | 0.04 | [32] |
| $d_{\mathrm{net}}$ | Aluminium cell size | nm | 370/520 | Present work Table 5 |
| $k_{(\mathrm{Si})}$ | Constant for effect of Si in solid solution | MPa/wt. $\%^{2/3}$ | 39.7 | [31] |
| $C_{\mathrm{Si}}$ | Si concentration in solid solution | wt. % | 2.4/1.6 | [8]/Equilibrium [33] |
| $\alpha$ | Material constant | - | 0.24 | [34] |
| $\rho_d$ | Initial dislocation density | $\mathrm{m}^{-2}$ | $1\times 10^{14}$ | [35] |
| $f_{\mathrm{net}}$ | Volume fraction of the Si-rich eutectic network | - | 0.12 | Equilibrium [36] |
| $\sigma_{\mathrm{load}}$ | Load bearing of the Si-rich eutectic network at the yield point | MPa | 380 | Derived from [28] using a Young's modulus of 112 GPa for Si [37] |

**Table 8**. Estimated strengthening components in 35°C and 200°C materials. The units are in MPa.

| $T_{\text{Build platform}}$ | $\sigma_0$ | $\Delta\sigma_{\mathrm{preci}}$ | $\Delta\sigma_{\mathrm{bound}}$ | $\Delta\sigma_{\mathrm{ss}}$ | $\Delta\sigma_{\mathrm{disloc}}$ | $f_{\mathrm{net}} \times \sigma_{\mathrm{load}}$ | **Estimated** $\sigma_y$ | **Measured** $\sigma_y$ |
|---|---|---|---|---|---|---|---|---|
| **35°C** | 10 | 158 | 66 | 71 | 37 | 46 | 347 | 286 |
| **200°C** | 10 | 44 | 55 | 54 | 37 | 46 | 222 | 203 |

Supplementary Material

# Influence on microstructure, strength and ductility of build platform temperature during laser powder bed fusion of AlSi10Mg

Juan Guillermo Santos Macías*, Thierry Douillard, Lv Zhao, Eric Maire, Grzegorz Pyka, Aude Simar

This supplementary material is devoted to clarify the parameter selection for the strengthening models presented in table 7 of the paper. Note that part of the parameters was experimentally determined by the authors; the rest was taken from the literature or estimated with reasonable inference.

The friction stress $\sigma_0$, which corresponds to the intrinsic yield strength of pure aluminium, has a typical value of 10 MPa [i]. This item was sometimes omitted in the strengthening analysis or modeling of high strength aluminium alloys [ii].

The Taylor factor $M$ presents a value of 3 by definition ($M = \sigma/\tau = \gamma_\mathrm{p}/\varepsilon_\mathrm{p}$) for FCC metals without texture. However, it has been argued by Deschamps and Bréchet [i] that using $M$ = 2 would be more appropriate even in the presence of slight texture. In fact, the grains are not fully constrained at the yield point, i.e., very low strains, deformations are thus not necessarily compatible and a homogeneous stress hypothesis can be applied. Note that $M$ = 2 has also been adopted in micromechanical modeling of mechanical properties of 6XXX, 7XXX [iii] and SLM AlSi10Mg [iv] Al alloys, allowing to capture the experimental results more accurately. The values of the shear modulus $G$ (27 GPa) and the amplitude of Burger's vector $b$ (0.284 nm) adopted in the present work were widely used in micromechanical modeling of Al alloy strength [ii, iii].

Regarding the fine Si precipitates (equivalent diameter $d_\mathrm{preci}$ and volume fraction $f_v$) present in the α-Al phase, their average size and volume fraction were measured using TEM (featured in our previous work [v]) and FIB/SEM tomography (present work) for the 35°C and 200°C materials, respectively. The resolution of the TEM images was approximately 0.3 nm, and the resolution of the FIB/SEM volumes was 5 nm. Note that the equivalent diameter of the Si precipitates of the 200°C alloy measured in the present work was very close (60 nm vs. 61 nm) to that determined with TEM images for the same manufacturing parameters [vi].

The value of the constant of the Hall-Petch relation, $k_d = 0.04\ \mathrm{MPa} \cdot \mathrm{m}^{1/2}$, was taken from Hansen [vii], who obtained it with a grain size range from about 20 nm to hundreds of micrometers. The average size of the aluminium cells, $d_\mathrm{net}$, was meticulously measured with the FIB/SEM tomography data, as presented in Table 5 of the main manuscript.

Concerning the solid solution, the constant $k_{(\mathrm{Si})}$ takes the value used for modeling the solid solution strengthening in AA6005 [iii]. The Si concentration $C_{(\mathrm{Si})}$ in the 35°C material was measured by TEM for the same material manufactured with the same machine and parameters [v]; for the 200°C material, the Si concentration was assumed to correspond to the equilibrium state, which is a lower bound of the solid solution strengthening effect. In fact, the 35°C material presenting the Si concentration of 2.4 wt. % is expected to be further from the equilibrium state, the assumption of the Si concentration of 1.6 wt. % is therefore tenable for the 200°C material.

The material constant α = 0.24 involved in the dislocation forest strengthening model was taken from Huang et al. [viii]. 0.24 is a good estimate of this empirical parameter for dislocation density in the $10^{13} - 10^{14}\ \mathrm{m}^{-2}$ range [ix]. The dislocation density was taken from Hadadzadeh et al. [x], who measured it by TEM on samples manufactured with the same parameters as our 200°C material. The relatively high dislocation density ($10^{14}\ \mathrm{m}^{-2}$) is likely due to the thermal strain incompatibility between the Al and Si phases (both network and precipitates) during repeated heating and cooling cycles. Note that no distinction in dislocation density is made between the

35°C and 200°C materials since no data can be found for material close to the 35°C case in the present work.

The volume fraction of the Si-rich eutectic network was assumed to be equal to that at equilibrium. The stress in the Si phase at the yield point was estimated with the strain measured by neutron diffraction [xi] and the Young's modulus (112 GPa) taken from Tang and Pistorius [xii]. It should be noted that the Young's modulus adopted by Kim et al. [xi] was too low (79.4 GPa) for the stress evaluation. It is worth mentioning that the Si-rich eutectic phase exhibits a considerable portion of amorphous volume according to the TEM diffraction pattern for the same sample [xiii]. As the polycrystalline Si presents a Young's modulus around 160 GPa [xiv] and the amorphous Si has a much lower modulus of 89 GPa [xv], the effective modulus of 112 GPa appears reasonable for evaluating the load bearing effect of the Si-rich phase.

## References

[i] A. Deschamps, Y. Bréchet, Influence of predeformation and ageing of an Al–Zn–Mg alloy—II. Modeling of precipitation kinetics and yield stress, Acta Mater. 47 (1999) 293-305.

[ii] O.R. Myhr, O. Grong, H.G. Fjaer, C.D. Marioara, Modelling of the microstructure and strength evolution in Al-Mg-Si alloys during multistage thermal processing, Acta Mater. 52 (2004) 4997-5008.

[iii] A. Simar, Y. Bréchet, B. De Meester, A. Denquin, T. Pardoen, Sequential modeling of local precipitation, strength and strain hardening in friction stir welds of an aluminum alloy 6005A-T6, Acta Mater. 55 (2007) 6133-6143.

[iv] X.P. Li, G. Ji, Z. Chen, A. Addad, Y. Wu, H.W. Wang, J. Vleugels, J. Van Humbeeck, J.P. Kruth, Selective laser melting of nano-TiB2 decorated AlSi10Mg alloy with high fracture strength and ductility, Acta Mater. 129 (2017) 183-193.

[v] L. Zhao, J.G. Santos Macías, L. Ding, H. Idrissi, A. Simar, Damage mechanisms in selective laser melted AlSi10Mg under as built and different post-treatment conditions, Mater. Sci. Eng. A 764 (2019) 138210.

[vi] A. Hadadzadeh, B.S. Amirkhiz, M. Mohammadi, Contribution of $Mg_2Si$ precipitates to the strength of direct metal laser sintered AlSi10Mg, Mater. Sci. Eng. A 739 (2019) 295-300.

[vii] N. Hansen, Hall-Petch relation and boundary strengthening, Scr. Mater. 51 (2004) 801-806.

[viii] T. Huang, L. Shuai, A. Wakeel, G. Wu, N. Hansen, X. Huang, Strengthening mechanisms and Hall-Petch stress of ultrafine grained Al-0.3%Cu, Acta Mater. 156 (2018) 369-378.

[ix] N. Hansen, X. Huang, Microstructure and flow stress of polycrystals and single crystals, Acta Mater. 46 (1998) 1827-1836.

[x] A. Hadadzadeh, B.S. Amirkhiz, J. Li, A. Odeshi, M. Mohammadi, Deformation mechanism during dynamic loading of an additively manufactured AlSi10Mg_200C, Mater. Sci. Eng. A 722 (2018) 263-268.

[xi] D. Kim, W. Woo, J. Hwang, K. An, S. Choi, Stress partitioning behavior of an AlSi10Mg alloy produced by selective laser melting during tensile deformation using in situ neutron diffraction, J. Alloy. Compd. 686 (2016) 281-286.

[xii] M. Tang, P.C. Pistorius, Anisotropic mechanical behavior of AlSi10Mg parts produced by Laser Powder Bed Fusion, JOM 69 (2017) 516-522.

[xiii] W. Lefebvre, G. Rose, P. Delroisse, E. Baustert, F. Cuvilly, A. Simar, Nanoscale periodic gradients generated by laser powder bed fusion of an AlSi10Mg alloy (Under revision).
[xiv] L. Zhao, A. Maynadier, D. Nelias, Stiffness and fracture analysis of photovoltaic grade silicon plates, Int. J. Solids Struct. 97-98 (2016) 355-369.
[xv] M.D. Kluge, J.R. Ray, Elastic constants and density of states of a molecular-dynamics model of amorphous silicon, Phys. Rev. B 37 (1988) 4132-4136.